Journal of The Electrochemical Society

The Electrochemical Society
Advancing solid state & electrochemical science & technology

Molecular Dynamics Study of Reaction Conditions at Active Catalyst-Ionomer Interfaces in Polymer Electrolyte Fuel Cells

To cite this article: Victor M. Fernández-Alvarez *et al* 2022 *J. Electrochem. Soc.* **169** 024506

Journal of The Electrochemical Society, 2022 **169** 024506
1945-7111/2022/169(2)/024506/8/$40.00 © 2022 The Author(s). Published on behalf of ECS by IOP Publishing Limited

Molecular Dynamics Study of Reaction Conditions at Active Catalyst-Ionomer Interfaces in Polymer Electrolyte Fuel Cells

Victor M. Fernández-Alvarez,[1] Kourosh Malek,[2] Michael H. Eikerling,[2,*] Alan Young,[3] Monica Dutta,[3] and Erik Kjeang[1,*,z]

[1]*Fuel Cell Research Laboratory (FCReL), School of Mechatronic Systems Engineering, Simon Fraser University, Surrey, BC V3T 0A3, Canada*
[2]*Theory and Computation of Energy Materials (IEK-13), Institute of Energy and Climate Research, Forschungszentrum Jülich GmbH, 52425 Jülich, Germany*
[3]*Ballard Power Systems, Burnaby, BC V5J 5J8, Canada*

Understanding the local reaction conditions at the catalyst-ionomer interfaces inside of polymer electrolyte fuel cells is vital for improving cell performance and stability. Properties of the water film and distributions of protons and oxygen molecules at the catalyst-ionomer interface are affected by the state of the catalyst and support surfaces and the structure of the ionomer skin layer. In this work, the interfacial region between catalyst and support surface and ionomer skin is simulated using molecular dynamics. This water-filled nanopore model is constructed to study the impact of local charge density, density of sidechains at the ionomer layer, and water layer thickness on the water structure and electrostatic conditions in the pore as well as the transport properties of water, hydronium, and molecular oxygen at the interface. The analysis of the flooded pore model indicates that surface hydrophilicity, represented by water adsorption and the formation of an ordered water layer at the surface, is a major factor determining the interfacial proton density, ionomer sidechain mobility, and interfacial oxygen transport resistance. The results obtained can guide the design of new catalyst materials, where the hydrophilicity of the surface can be tailored to minimize the local proton transport resistance and improve electrode performance.

Manuscript submitted August 10, 2021; revised manuscript received January 11, 2022. Published February 1, 2022.

Polymer electrolyte fuel cells (PEFCs) are electrochemical energy conversion devices with major applications in on-site power generation and electric mobility. The latter in particular is an increasingly important sector, with PEFCs offering a zero-emission alternative to internal combustion engines with across light-duty, medium- commercial, and heavy-duty vehicle markets.[1–3] However, marked improvements in terms of cost, performance, and durability are still required for the full-scale commercialization of PEFCs. The high system cost is mainly driven by the cost of catalyst layer materials and components, in particular platinum needed as electrocatalyst for the oxygen reduction reaction (ORR) at the cathode. At low Pt loading, the effective activity of the cathode catalyst layer (CCL) for the ORR is significantly affected by transport resistance phenomena, as well as catalyst degradation.[4–7] Thus, it is vital to understand the factors governing transport phenomena in the CCL in order to improve its performance.[8,9]

The conventional CCL consists of Pt catalyst nanoparticles that are supported on a carbon-based nanoporous support material. Aggregates of Pt/C particles are covered with an ion-conducting polymer, usually Nafion ionomer. Improving the fuel cell designs for low cost, high performance and high stability requires reduced Pt content, optimal statistical utilization of Pt, and highly uniform reaction conditions inside of the CCL for a broad range of operating conditions. These requirements entail improving reactive transport processes at the polymer-catalyst interface. It has been suggested that at high operating current density, mass transport losses and, in particular, an oxygen transport resistance causes significant reductions in power output.[4,7,10,11] The oxygen transport resistance can originate in the gas diffusion layer, microporous layer, or CCL, with the precise origin still being a matter of debate.

The CCL constitutes a difficult space to explore using theory and computation and the most challenging fuel cell component to study experimentally.[8,12] Four phases must be distinguished, including the solid phase of Pt and carbon, the ionomer phase, a liquid water phase and a gas phase. The latter two phases coexist in a complex pore network that typically exhibits a bimodal pore size distribution and highly heterogeneous wetting conditions. The liquid saturation in the layer is a function of operating parameters. Therefore, the volumetric composition in terms of the four phases as well as effective parameters of transport and reaction in the CCL are variable functions of operating parameters as well.[13,14] On the one hand, water is essential as a proton solvent and only fractions of the Pt surface that are wetted by liquid water will be electrocatalytically active for the ORR. On the other hand, water that is generated during operation could cause excessive flooding of pores that are required for the gaseous supply of oxygen. This flooding effect could incur significant losses in the fuel cell voltage due to the inhibited transport of oxygen in water.[15] Due to the small scale and porous nature of the CL, experimental observation of the CCL region remains difficult,[16] and models of PEFCs often approximate the CCL to an infinitesimally thin layer,[17,18] or they do not explicitly distinguish the water phase in CCL.[19] However, water phenomena must be rationalized and monitored at all structural levels and in all components of the cell. Here we focus on water phenomena at the microscopic scale, considering a slab of water that is confined by the walls of the solid phase on one side and the ionomer phase on the other side. We rationalize in molecular-level detail the structure of this water layer and the density distributions of excess protons and oxygen molecules in it. This understanding thus reveals the local reaction conditions that are responsible for the ORR activity and the dissolution kinetics of the catalyst.

Computational models have become an essential part of CCL investigation as they can offer insights at the molecular level, out of reach for most experimental setups.[20,21] Recently, molecular dynamics (MD) models of the CL have been developed to study the structure of the catalyst-ionomer interface,[22,23] and oxygen transport through the ionomer thin film.[24] Tokumasu et al. carried out MD simulations of a cross-section of the CCL, and argued that within the CCL, the interface plays an important role contributing to oxygen transport resistance.[25] Most computational models based on molecular dynamics that focus on transport treat the C and Pt surfaces as ideal pristine surfaces. Yet we know that at typical electrode potentials for the ORR both surfaces become partially oxidized, which not only alters the surface charge properties of the catalyst surface,[26] but also the interactions with and configuration of interfacial water molecules around them.[27–29] Moreover, the equilibrium structure of interfacial water molecules can alter the morphology of the ionomer at the interface.[16,30] The effects of electrode

*Electrochemical Society Member.
[z]E-mail: ekjeang@sfu.ca

potential on the structure of the interface have been studied recently using ab initio methods.[31,32] However, the high computational cost of ab initio simulations prevents the modelling of system with a significant amount of water molecules and a layer of ionomer molecules present at the interface.

An MD model of the catalyst-ionomer interface was recently developed, in which the surface of Pt(111) was evaluated at varying oxide coverage to study the proton behavior.[33] That model was also used to compare the oxidized Pt(111) and Pt(100) surfaces and their resulting interfacial water structure.[34] In the present work, this model is modified to study the catalyst-ionomer interface of both functionalized graphite and oxidized Pt(111). The objective is to understand how the properties of the support material determine the structure of interfacial water molecules and ionomer, and to, furthermore, rationalize the effect the resulting water layer has on properties that determine the CCL performance. By modifying the parameters of the model, the impact of surface functionalization on water ordering, ionomer sidechain mobility, and proton dynamics are investigated. In addition, molecular oxygen diffusivity at the interface is analysed by comparing the graphite support surface with the Pt(111) catalyst surface.

This article is organized as follows: the details of the model system and the methodology used for the molecular dynamics simulations is described in the next section. The discussion section is itself divided into three subsections, covering hydronium density accumulation at the surface, ionomer sidechain dynamics, and in-plane oxygen diffusivity at the interface. Finally, the general insights obtained from the model are summarize in the conclusions section.

Methodology

The 3D model system (Fig. 1) used for the MD simulations consisted of a water-filled slab-shaped nanopore. The water region was confined by two square-shaped 10 × 10 nm boundary surfaces, comprised of a graphite or platinum slab and a skin layer of ionomer. The separation between the two bounding surfaces, determining the thickness of the water slab in-between, is tuneable. The resulting system thus effectively employed fixed boundary conditions in the direction normal to the surface and periodic boundary conditions in the direction parallel to the surface. The simplified ionomer model consisted of a layer of equidistant and uniformly distributed -CF axis groups that remained fixed in their position during simulations. These groups were connected to free-moving Nafion sidechains and a chain of -CF_2 backbone. The length of the -CF_2 backbone chains was determined by the equivalent weight of the ionomer units. Due to the hydrophobic nature of the -CF_2 chains, the backbone sections arranged themselves away from the water layer during simulation, mimicking the outer face of a lamellar ionomer structure, and served as the upper limit of the simulation region. The working hypothesis behind this constraint is that in aqueous media, the backbone chains tend to link together in clusters while the hydrophilic sidechains point outwards toward the water region.[35] The slab region consisted of water, hydronium, and oxygen molecules (Fig. 1). The oxygen concentration was set at 8×10^{-5} mol cm^{-3} (40 oxygen molecules), which is higher than normal values. Computation of diffusion coefficients from molecular dynamics simulations requires linear mean-squared displacement plots, and to reach that linearity, the oxygen concentration was increased three-fold from the normal concentration. It is assumed that any effect this high concentration may have on diffusion coefficients is systematic and does not affect comparative values between different simulation conditions. The hydronium ion concentration was adjusted to match the number of sidechains in the ionomer layer for overall electroneutrality in the system. The total charge at the catalyst and support surface was zero. However, upon oxidation a partial charge density distribution is developed between the oxide and C/Pt atoms as a result of the electronic structure calculation. The properties of the model were studied by changing the four parameters listed in Table I. Oxide coverage of both platinum and carbon (θ) matched that found in the potential range from 0.3 to 0.9 V, although it is not directly analogous to potential as the surface charge density is not described in its entirety. The surface density of ionomer sidechains (σ^S) was tuned to the density range found at pore walls for the range of ionomer equivalent weights between 1193 a [illegible] was varied by modifying the structure, number, and intermolecular distance of ionomer units in the simulation cell. Finally, the thickness of the water region that separates the ionomer layer from the catalyst/support surface (d) was modified by adjusting the position of the ionomer axis points in the simulation cell and flooding the space between ionomer and surface with water molecules pre and post initial equilibration.

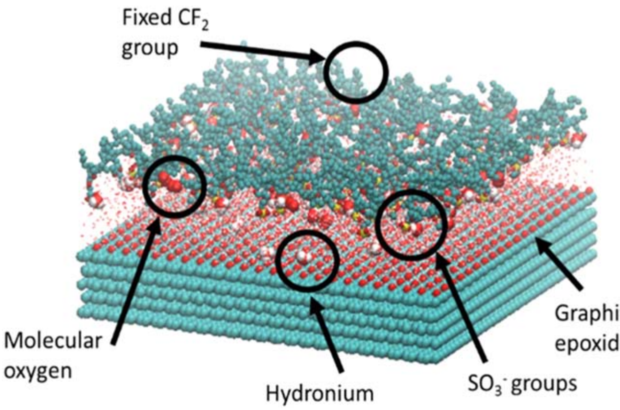

Figure 1. Interfacial system with the water slab confined between the solid surface (of Pt or C) and the ionomer skin layer. Snapshot from molecular dynamics simulation.

The C support surface was modelled as five graphene layers arranged in alternate positions forming a graphite slab. Atomic positions and surface charge densities for slabs at varying oxide coverages were obtained from periodic Density Functional Theory (DFT) calculation for the graphite oxide layer at zero total charge. The bottom two layers were kept fixed in position while the top three layers were fully relaxed during geometry optimization. The oxidized Pt surface was built as a five-layer Pt slab with (111) facet structure with oxide coverage varying from 6 to 70% O/Pt ratio. In both carbon and Pt surfaces, all three top layers were allowed to relax while the bottom two layers were kept fixed. DFT calculations were carried out using the Vienna Ab initio Simulation Package (VASP).[36] The generalized gradient approximation (GGA) with the revised Perdew–Burke–Ernzerhof (revPBE) exchange correlation functional was used,[37] and valence electrons were treated with the projector augmented wave (PAW) method.[38] The cut-off energy of the plane wave expansion was 400 eV. A 4 × 4 × 1 Monkhorst-Pack k-point mesh was used to sample the Brillouin zone. According to the Lerf-Klinowski model,[26] graphene sheets are functionalized with hydroxyl and epoxide groups, while edges and rough surfaces favor carboxyl groups.[31] For reasons of simplicity in the interpretation of results, only one type of functional group was added in each simulation. Experimental evidence indicates functionalization varies from C/O ratios of 10:1 to 2:1.[30] Therefore, functionalized graphite slabs were optimized at 12.5, 25, and 50% for graphite epoxide and 12.5 and 25% for hydroxyl epoxide, as 50% hydroxyl coverage was not stable and collapsed during DFT optimization. Experimental measurements of carbon black functionalization favor the formation of both hydroxyl and epoxide at the surface upon cycling and during operation.[39] Partial charges were added from Bader charges, obtained via the partial charge distribution that results form DFT calculations, following the model construction protocol of previous work.[33]

A polymer skin layer that consists of a square-shaped array of identical ionomer units with flexible sidechains and a constrained backbone network was added at the top of the simulation box. United atom representation was used for CF_3, CF_2, and CF, while S

Table I. Parameters of the model.

Variable	Symbol (unit)	Range
Graphite oxide species	—	Epoxide and hydroxyl
Graphite oxide coverage	θ	0%-50%
Platinum oxide coverage	θ	6.25%-69%
Ionomer sidechain number density	σ^S (nm^{-2})	1.05–2.10
Water layer thickness	d (nm)	0.5–2.5

and O in the sidechain were treated using a full atomistic model. The distance between side chain groups was controlled and held constant by fixing the CF group at the junction of the sidechain and backbone. These junction groups were fixed to their initial positions during the MD simulations, maintaining the array structure and prohibiting any major restructuring of the film. The model system assumes the formation of a water layer between the ionomer and the catalyst surface, as discussed in previous reports.[22,33] Real densities of ionomer sidechains were varied from 1.05 nm^{-2} to 2.10 nm^{-2} in this work to evaluate the effects of ionomer properties on the molecular structure and distribution water, hydronium ions, and oxygen at the interface. The polymer surface used in the simulations had dimensions of 10 × 10 nm, matching the size of the solid surface, and contained between 105 and 210 individual ionomer units. Figure 2A shows a section of the model system, where functionalized graphite epoxide is the support surface. Above the graphite slab, in the X direction, lies the water layer region, which ends at the ionomer skin-layer that bounds the system from above. Water saturation of the CCL during operation caused by current generation has been studied using small-angle neutron scattering, and water uptake values in the cathode higher than 20 were observed.[40] This water was mostly confined to a relatively small region at the interface, of roughly 15 Å thickness.[41] The flooding of the pore in the present simulation cell aims to reproduce this saturation effect during operation.

Initial state configurations of the model system were run for a total of 18 ns, divided into 6 ns of thermalization and 12 ns of production run. Structural analysis was carried out using trajectory frames every 1000 steps. Angular distributions were obtained using MDAnalysis package,[42] radial distribution functions were calculated using VMD,[42] and every other property was computed using GROMACS tools.

The conditions for the molecular dynamics calculations have been described in previous work.[33] MD simulations were performed in the canonical (NVT) ensemble using the GROMACS package,[43,44] using the V-rescale thermostat to keep the system at a constant temperature of 300 K,[45] with relaxation time of 0.1 ps. MD trajectories were computed via leap-frog integration with 1 fs time step and a direct space interaction cut-o nm. Long-range electrostatic interactions were calculated with the particle mesh Ewald (PME) technique,[46] using the slab correction (3dc) for surface systems.[47] Periodic boundary conditions were applied in the x and y dimensions (parallel to the bounding surfaces). We used the Single Point Charge model for water.[48,49] The water slabs between polymer surface and PtO were constructed using the GROMACS tool genbox. The total number of water molecules varied according to the imposed thickness of the water layer (defined as the distance between the C/Pt surface and the ionomer layer "d") and ranged from about 3000 for $d = 0.5$ nm to 10000 molecules for $d = 3.5$ nm. Molecular oxygen was described using GROMOS 54A7 parameter

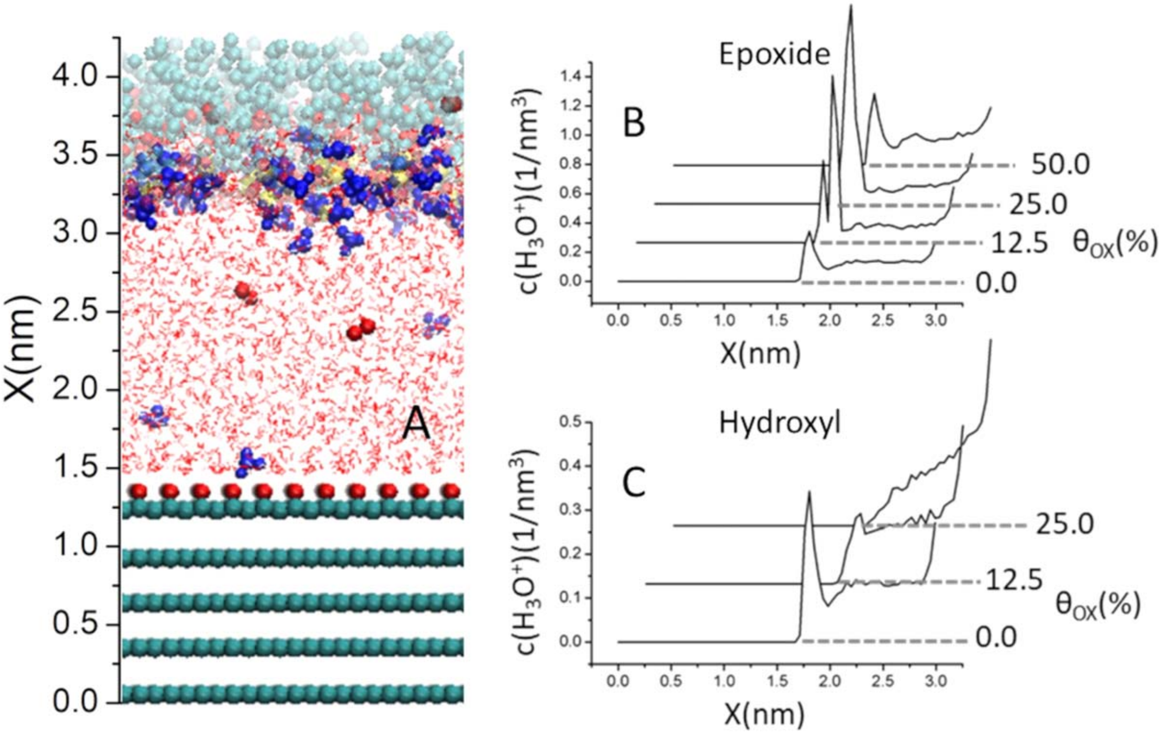

Figure 2. Snapshot representation of a section of the simulation box (A) using a 2 nm water layer thickness. Plane-averaged hydronium ion linear density at graphite epoxide (B) and graphite hydroxyl (C) in the vicinity of the graphite oxide surface. Water layer thickness $d = 2.0$ nm, and ionomer sidechain density $\sigma^S = 1.05$ nm^{-2}.

set.[50] Atomic force field parameters for carbon, oxygen, and hydrogen in graphite were taken from Keffer et al.[25] Atomic force field parameters for ionomer, full atomistic hydronium, and PtO species can be found in our previous publication.[33]

Results and Discussion

The following subsections analyze the effect of graphite surface functionalization on the structure of interfacial water molecules and ionomer, and how the transport properties relevant for cathode catalyst layer performance are affected by it. The surface structures analyzed were pristine graphite, graphite epoxide between 12.5% and 50% coverage, and graphite hydroxyl between 12.5% and 25% coverage. In the case of oxygen lateral diffusion analysis, the oxidized Pt(111) surface was studied as well to compare the effect of interfacial water structure between the catalyst and support materials.

Proton adsorption at the graphite surface.—To analyze the proton density distribution in the system, the water layer thickness was kept sufficiently large (2.0 nm) to differentiate density accumulation at the graphite surface from that at the ionomer region. The plane-averaged linear density of hydronium ions was used to analyze the interaction and adsorption of hydronium ions at the functionalized graphite surface, where the normal direction to the surface was chosen as the density coordinate. Previously, published results showed a pronounced oxide-induced enhancement of the hydronium ion density at the Pt(111) surface, using an otherwise identical model.[33] As expected, hydronium ion accumulation was predominantly localized around the sulfonate groups in the ionomer side-chains (not shown), ion-ion interactions being far stronger than ion-dipole interactions. Yet, Figs. 2B and 2C reveal a discernible accumulation of hydronium ions at the surface of graphite oxide; this concentration increase is highly dependent on both the type and degree of functionalization, represented as oxide coverage. Figure 2B shows that there is an increase of the hydronium ion density at the graphite epoxide surface, which is caused by the electrostatic attraction of hydronium ions to the negative partial charge of the epoxide groups. Conversely, graphite hydroxyl shows no hydronium ion accumulation at the surface (Fig. 2C), which is attributed to electrostatic repulsion between hydronium ions and the protic hydrogen in the hydroxyl groups. As a result of this electrostatic repulsion, hydronium interacts with the ordered water layers near the hydroxyl surface, and not with the surface functional groups directly (Figs. 3B and 3C). The accumulation of hydronium ions at the graphite epoxide surface is not constant with increasing functionalization, as evidenced by the varying linear density peak values in Fig. 2B. The accumulation effect is only significant (more than one molecule per cubic nm) at partial oxide coverage, with density peaks at the surface decaying in intensity from 12.5% to 25% and finally disappearing at 50%. Figure 2A shows that hydronium ion adsorption takes place at the epoxide centers, suggesting that larger coverage should lead to greater hydronium ion surface density. However, hydronium density peaks at the graphite epoxide surface are only significant at partial functionalization. These changes in hydronium ion affinity can be rationalized by studying the structure of the water layer near the epoxide surface.

Figure 3A shows the angular distribution of water dipoles with respect to the normal direction of the slab in a slice of 3 Å thickness above the graphite epoxide surface. A broad peak around $\cos(\phi) = 0$ indicates a random water orientation, whereas a peak near 1 means most water dipoles are on average preferentially oriented in the normal direction to the surface, and peaks around 0.5 indicate a mixture of the two.[51] The graph indicates that both clean graphite and fully covered graphite epoxide show no preferred water orientation. The slab with 12.5% epoxide coverage shows the sharpest peak, located near 1, indicating strong ordering of water layers which favors dipole-ion interactions with hydronium, while the slab at 25% oxidation shows a lower degree of ordering which is reflected in a smaller hydronium density peak. He et al.[30] found that the preferred orientation of water molecul epoxidized graphite surface is the oxygen atom in direct contact with the positively charged carbon atoms in graphite and the hydrogens directed towards the epoxides, which corresponds to the angular distributions found in this work. It should be noted that 50% epoxide coverage implies all carbon atoms are epoxidized, which in turn means that there are no vacant positive carbon atoms to allow for this water orientation, resulting in a disordered water layer. The behavior of graphite epoxide towards water dipoles reveals that the pristine graphite surface, which is largely hydrophobic, becomes hydrophilic upon epoxidation, and this hydrophilic character diminishes with increased epoxide coverage until it virtually disappears at full coverage (50% C/O). This reduction of hydrophilicity with increased oxidation of the graphite surface has recently been observed using neutron reflectometry.[52] The change in hydrophilicity explains the presence of accumulated hydronium ions only at partial oxidation states.

Functionalization of the carbon support surface leads to a change in hydrophilicity, as the surface changes from hydrophobic graphite to hydrophilic graphite oxide. This in turn can be expected to affect the orientation and structure of the ionomer sidechains at the interface. Recent molecular dynamics studies showed that

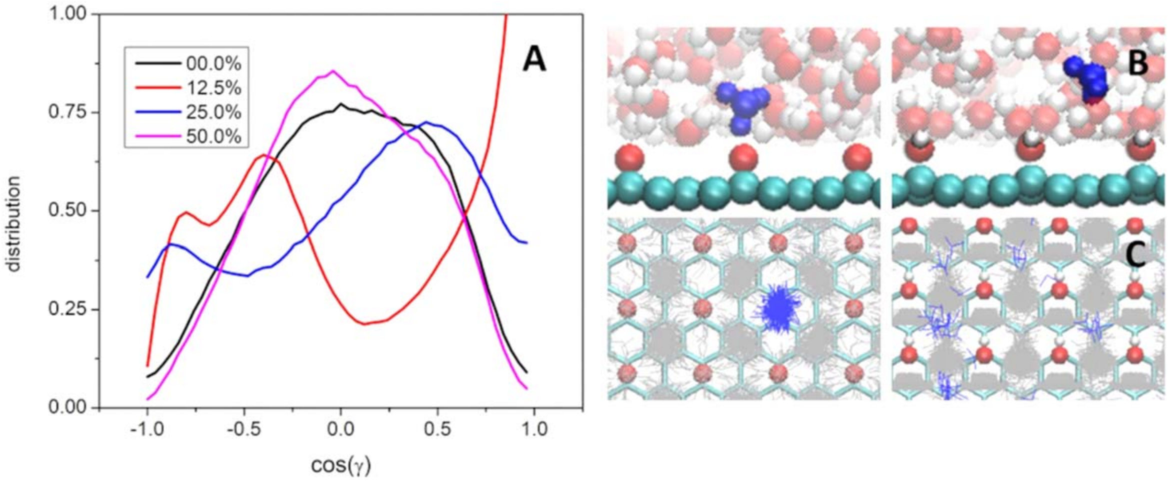

Figure 3. Hydronium preferred orientation. (A) Angular distribution function of interaction angle (γ) between water dipole moment and graphite epoxide surface plane. (B) Closest hydronium (blue) interaction with graphite epoxide (left) and hydroxyl (right) surfaces. (C) Hydronium (blue) and water (gray) density accumulation near the surface of graphite epoxide (left) and hydroxyl (right).

hydrophilic surfaces attract the ionomer sidechains while repelling the backbone, and this effect is reversed when the surface is modified to be hydrophobic.[53]

Ionomer dynamics at the interface with carbon support material.—Figure 4 shows that the carbon surface hydrophilicity affects the configuration of the ionomer, even in a restrictive model such as the skin ionomer layer studied here. Sidechain functional groups (Fig. 4A) and water molecules (Fig. 4B) are both repelled by clean graphite, while the partially epoxidized graphite shows a density peak of both water and sulphur accumulation at close range (r = 0.18–0.22 nm), which disappears at full oxidation. The effect of carbon functionalization on the structure of the ionomer has been observed experimentally.[54] Density peaks are an indicator of molecular density accumulation at a certain distance from the surface and can be interpreted as adsorption or coordination. Similarly, graphite hydroxyl showed density peaks for both water and sidechain functional groups near the surface at 12.5% and 25% coverage. Figure 4C shows the ionomer sidechain mobility, expressed as root mean square fluctuations, at all surface oxidation levels and its correlation with water self-diffusion for the case of graphite epoxide.

Water self-diffusion serves as another descriptor of hydrophilicity; since the ionomer sidechain density and water layer thickness are kept constant, the only factor influencing water self-diffusion is the degree of a preferred orientation of near-surface water molecules. The comparison with ionomer position fluctuations shows how the mobility of ionomer sidechains is restricted by the favorable interaction of water dipoles with the functionalized graphite surface. The case of graphite epoxide illustrates the impact of hydrophilicity (expressed as the affinity of water molecules to adsorb at the surface) on proton density accumulation and ionomer sidechain mobility at the interface. Increasing oxide coverage beyond 25% reduces the number of vacant surface carbon atoms, which are positively charged, and depolarizes the surface, reducing hydrophilicity.

He et al. rationalized that the absence of available positively charged carbon atoms at the surface hindered the coordination of ordered water molecules as the cause of the reduction in hydrophilicity with increased epoxide coverage.[30] This rationalization also helps explain the trend in ionomer sidechain mobility. Sidechain radial density peaks (Fig. 4B) are at 2.0–3.0 Å from the partially oxidized graphite surfaces, while water density peaks (Fig. 4A) are at 1.5–2.0 Å. The difference can be attributed to the fact that the sidechains are anionic and thus adsorbed at the hydrogen atoms of the ordered water layer, rather than directly at the negatively charged graphite epoxide. If there is no ordered water layer, the ionomer sidechains are not adsorbed at the surface, as observed for the pristine and fully oxidized graphite surfaces.

Oxygen in-plane diffusivity at the interface.—It remains an open debate whether the catalyst-ionomer interface contributes considerably to oxygen transport resistance in the CCL.[5,24] Regardless of the role of out-of-plane permeability to oxygen transport losses, resistance to oxygen diffusivity at the interface is expected to have an in-plane component, as oxygen moves along the interface to reach a reaction site. The analysis in this section focuses on the in-plane (lateral) diffusion of oxygen molecules in the water film.

Figure 5A shows the lateral diffusion coefficients obtained for oxygen at the interface with functionalized graphite or with Pt(111)-O.

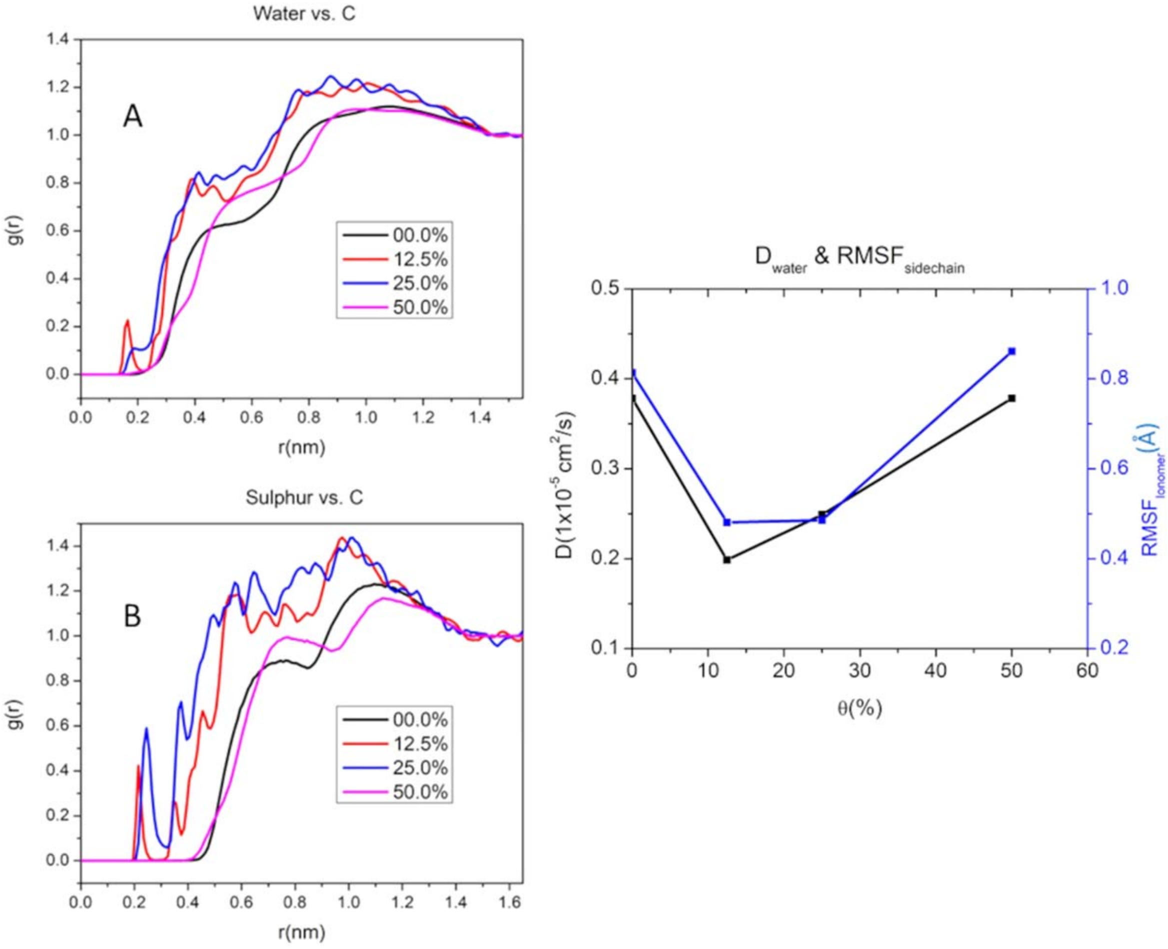

Figure 4. Radial distribution function (RDF) of water molecules (A) and sulphur atoms in ionomer sidechains (B) as a function of epoxide coverage on graphite. (C) Ionomer sidechain mobility as root mean square fluctuations (blue) and self-diffusion coefficient of water (black), as a function of epoxide coverage. Water layer thickness d = 0.5 nm, and ionomer sidechain density σ^S = 1.05 nm^{-2}.

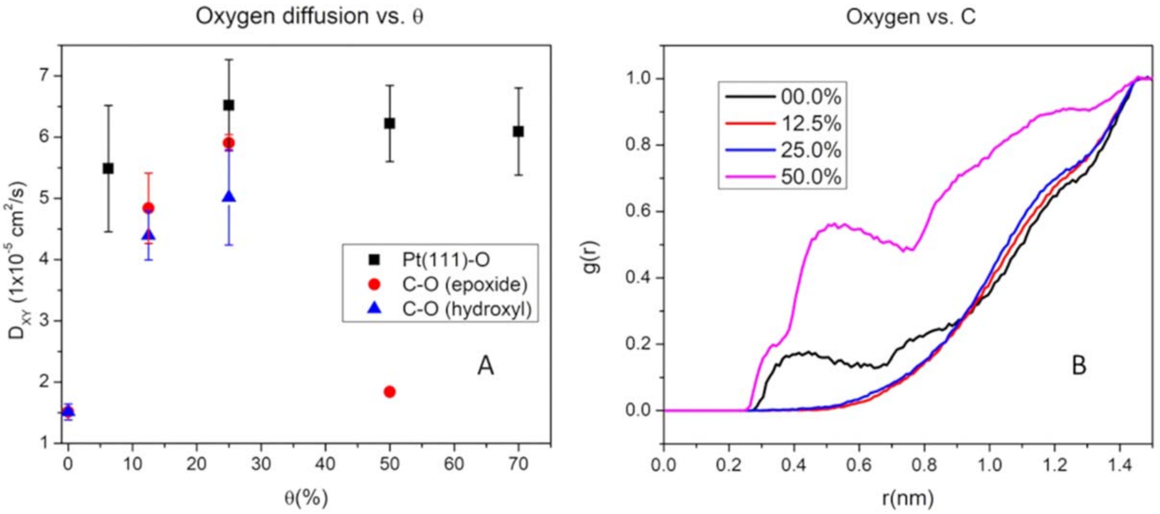

Figure 5. (A) Lateral diffusion coefficient of oxygen as a function of oxide coverage for Pt(111) (black), graphite epoxide (red), and graphite hydroxyl (blue). (B) Radial distribution function of molecular oxygen vs the surface graphite layer in graphite epoxide. Water layer thickness $d = 0.5$ nm, and ionomer sidechain density $\sigma^{S} = 1.05$ nm^{-2}.

While oxygen lateral diffusion is unaffected by the oxide coverage on platinum, as every Pt(111)-O surface is hydrophilic, the results for oxidized graphite show a strong correlation between lateral diffusion and the surface hydrophobicity. Specifically, partially oxidized, hydrophilic surfaces display fast lateral diffusion whereas pristine and fully oxidized hydrophobic surfaces restrict diffusion. Radial distribution functions (Fig. 5B) show that oxygen interacts favorably with hydrophobic surfaces such as graphite and fully oxidized graphite, whereas it is repelled by hydrophilic surfaces such as Pt and partially oxidized graphite. This repulsion results in faster oxygen movements as the mobility is not impeded by attractive interactions of oxygen molecules with the surface. While the hydrophilicity of the graphite surface significantly affects in-plane oxygen diffusion, the charge distribution at the surface shows no impact, as hydroxyl and epoxide graphite show nearly identical profiles in terms of oxygen lateral diffusion. It is important to note that this reduction of mobility at hydrophobic surfaces disappears in wider pores ($d > 2$ nm) (Fig. 6), where oxygen can move along the water region and the ionomer layer has higher mobility regardless of the surface.

Variations in sidechain density have an impact on oxygen lateral diffusion at hydrophilic surfaces. Figure 6A shows that partially oxidized graphite and Pt(111) have decreasing D_{XY} with increased sidechain density. The same effect has been observed experimentally on similar systems.[55] The thickness of the water slab was set at 1.5 nm to ensure minimal ionomer-catalyst interaction but to allow the hydrophilicity of the surface to impact oxygen movement. It was previously observed that hydrophilic surfaces create an ordered water layer which attracts the ionomer sidechains and hinders their movement, and Fig. 6 shows that they repel oxygen as well. This results in oxygen moving mostly near the ionomer skin layer, and that movement becomes hindered with increased sidechain density. Xiao et al. found that, by decreasing the hydrophilicity of the coating polymer in high temperature fuel cells, oxygen transport resistance at the interface was reduced.[56] A similar effect is observed in the present model system; by adding more sidechains, the hydrophilicity of the ionomer skin layer increases and oxygen movement through the ionomer region is reduced. Clean graphite, being hydrophobic, allows for oxygen to approach. This makes lateral diffusion less dependent on the behavior of the ionomer. This effect becomes apparent when compared with ionomer sidechain mobility. Figure 6B shows that ionomer fluctuations are reduced when sidechain density increases regardless of surface structure, indicating that the ionomer region at the interface is more congested in each case. The affinity of molecular oxygen for hydrophobic surfaces makes its mobility less sensitive to sidec in pristine graphite. At high sidechain density (Fig. 6C), oxygen lateral diffusion is largely independent of pore width.

Conclusions

This work applied molecular dynamics simulations to the model of a water-filled slab confined between an ionomer skin layer and a solid surface of carbon support or platinum. The simulations aim to explore the effects of the surface functionalization on water and proton dynamics as well as oxygen diffusivity. It was found that the variations in surface hydrophilicity that is imposed by graphite functionalization with epoxide and hydroxyl groups, and the resulting interfacial water layer structure, are major factors affecting local proton density in flooded pores. Moreover, the preferential orientation of interfacial water molecules affects the mobility of ionomer sidechains near the surface, with more hydrophilic surfaces creating an oriented water layer that attracts the sidechains near the support material. The degree and type of functionalization also has an impact on local transport properties. Epoxidation results in increased hydrophilicity only at partial coverage between 12.5 and 25%. Full coverage blocks the positively charged carbon centers and prevents water molecules from arranging in a favorable configuration to result in preferential dipole orientation, resulting in low hydrophilicity. This results in a disordered configuration of near surface water molecules, and the suppression of hydronium ion accumulation and increases ionomer sidechain mobility. In addition, hydroxylation results in water ordering, but the charge distribution of hydroxyl groups repels hydronium ions and prevents their accumulation at the surface. Therefore, not only surface hydrophobicity but also surface charge distribution determine the accumulation of hydronium at the functionalized support surface. Mobility of ionomer sidechains is similarly affected by hydrophilicity, yet it is unaffected by surface charge distribution, as sulfonic groups interact with the adsorbed water layer rather than directly with the surface functional groups.

Lateral oxygen diffusion properties were also found to be highly dependent on the hydrophilicity of the surface. In narrow pores at hydrophobic surfaces, oxygen diffusion is slowed by the attractive (and thus immobilizing) interaction with the support material, while being largely indifferent to sidechain density in the ionomer layer. Conversely, at hydrophilic surfaces, oxygen is repelled by the ordered water molecules and moves predominantly near the ionomer backbone layer, away from the surface. In the case of PtO, the surface is hydrophilic regardless of the partial oxide coverage, which

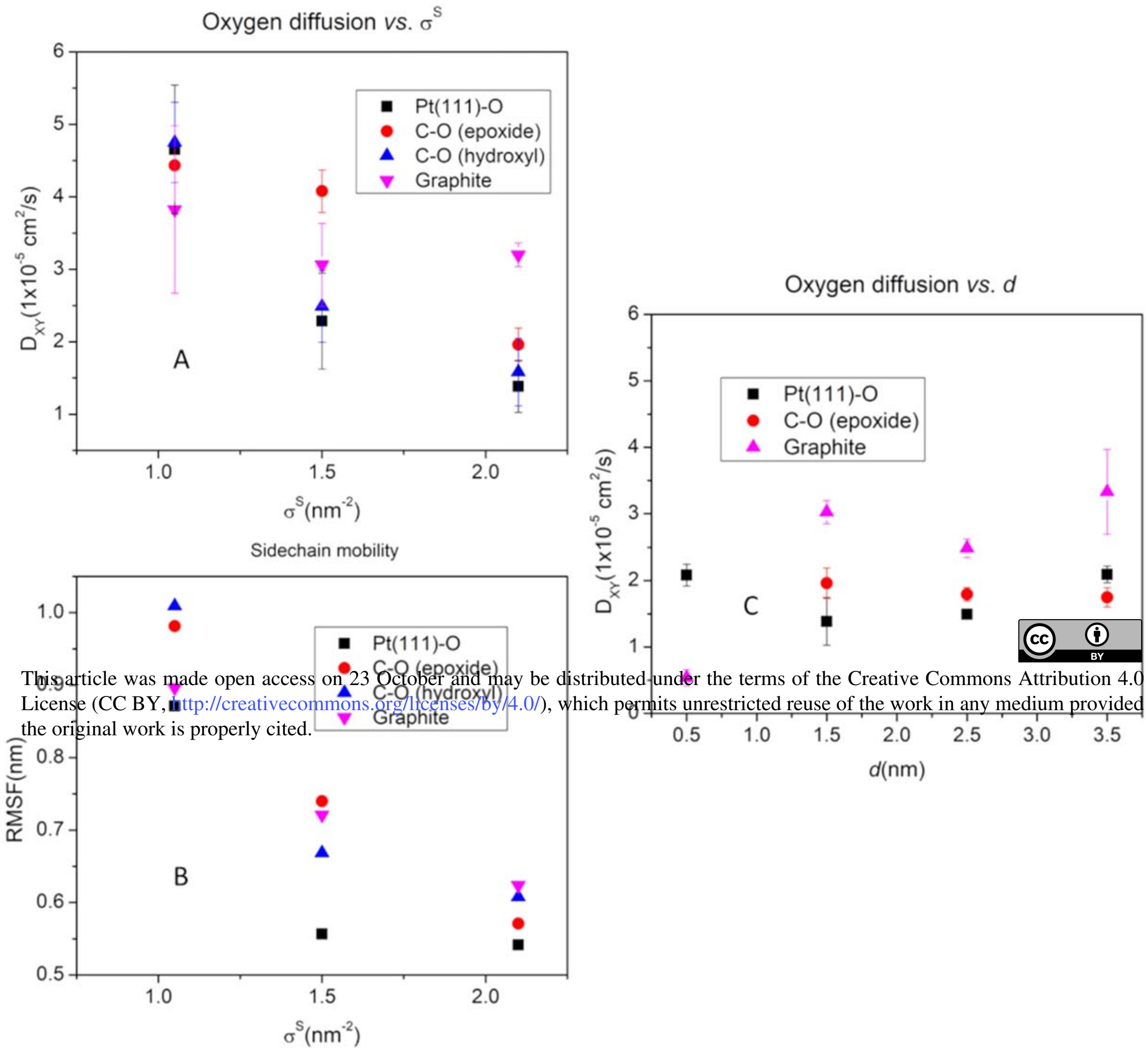

Figure 6. (A) Lateral diffusion coefficient of molecular oxygen for Pt and graphite surfaces vs ionomer sidechain density. (B) Ionomer mobility as root mean square fluctuations vs ionomer sidechain density. Water thickness $d = 1.5$ nm; oxygen coverage 50% for Pt(111) (black), 25% for graphite epoxide (red) and hydroxyl (blue), and 0% for graphite (purple). (C) Lateral diffusion coefficient of molecular oxygen for Pt and graphite surfaces vs water layer thickness. Sidechain density $\sigma^S = 2.1$ nm^{-2}; oxygen coverage 50% for Pt(111) (black), 25% for graphite epoxide (red), and 0% for graphite (purple).

results in oxygen moving predominantly along the ionomer layer. At hydrophilic surfaces, a higher sidechain density results in hydrophilic pockets of coordinated water molecules in the ionomer region, preventing oxygen movement through it. This dependence is only apparent at narrow pores (<1.5 nm), as increasing the water layer thickness leads to oxygen moving through the larger bulk-like water region and away from both boundary regions. The insights obtained in this work regarding the impact of surface hydrophilicity on local transport properties, particularly local oxygen diffusion at the interface, could aid the design of future catalyst / support systems by manipulating the affinity of molecular oxygen for hydrophobic surfaces, thus minimizing inefficiencies in oxygen supply to the catalyst. Similarly, controlling the hydrophilicity of the support material and the nature of the surface functional groups, can induce shifts in hydronium ion density at the surface, with important implications for the activity of the catalyst for the oxygen reduction reaction.

Acknowledgments

Funding from Natural Sciences and Engineering Research Council of Canada, Canada Foundation for Innovation, and British Columbia Knowledge Development Fund is appreciated. This research was undertaken, in part, thanks to funding from the Canada Research Chairs program. Victor M. Fernandez-Alvarez would like to acknowledge Mitacs and Ballard Power Systems for funding and support of this work. This research was enabled in part by support provided by Westgrid (www.westgrid.ca) and Compute Canada (www.computecanada.ca).

ORCID

Erik Kjeang https://orcid.org/0000-0002-1373-5212

References

1. H. Chen, Z. Song, X. Zhao, T. Zhang, P. Pei, and C. Liang, "A review of durability test protocols of the proton exchange membrane fuel cells for vehicle." *Appl. Energy*, **224**, 289 (2018).
2. O. Z. Sharaf and M. F. Orhan, "An overview of fuel cell technology: Fundamentals and applications." *Renew. Sustain. Energy Rev.*, **32**, 810 (2014).
3. Y. Wang, K. S. Chen, J. Mishler, S. C. Cho, and X. C. Adroher, "A review of polymer electrolyte membrane fuel cells: technology, applications, and needs on fundamental research." *Appl. Energy*, **88**, 981 (2011).
4. R. K. Ahluwalia, X. Wang, J. Kwon, A. Rousseau, J. Kalinoski, B. James, and J. Marcinkoski, "Performance and cost of automotive fuel cell systems with ultra-low platinum loadings." *J. Power Sources*, **196**, 4619 (2011).
5. D. R. Baker, D. A. Caulk, K. C. Neyerlin, and M. W. Murphy, "Measurement of oxygen transport resistance in PEM fuel cells by limiting current methods." *J. Electrochem. Soc.*, **156**, B991 (2009).

6. K. Karan, "PEFC catalyst layer: recent advances in materials, microstructural characterization, and modeling." *Current Opinion in Electrochemistry*, **5**, 27 (2017).
7. A. Ohma, T. Mashio, K. Sato, H. Iden, Y. Ono, K. Sakai, K. Akizuki, S. Takaichi, and K. Shinohara, "Analysis of proton exchange membrane fuel cell catalyst layers for reduction of platinum loading at Nissan." *Electrochim. Acta*, **56**, 10832 (2011).
8. T. Jahnke et al., "Performance and degradation of proton exchange membrane fuel cells: state of the art in modeling from atomistic to system scale." *J. Power Sources*, **304**, 207 (2016).
9. S. Woo, S. Lee, A. Z. Taning, T.-H. Yang, S.-H. Park, and S.-D. Yim, "Current understanding of catalyst/ionomer interfacial structure and phenomena affecting the oxygen reduction reaction in cathode catalyst layers of proton exchange membrane fuel cells." *Current Opinion in Electrochemistry*, **21**, 289 (2020).
10. P. Gazdzicki, J. Mitzel, A. M. Dreizler, M. Schulze, and K. A. Friedrich, "Impact of platinum loading on performance and degradation of polymer electrolyte fuel cell electrodes studied in a rainbow stack." *Fuel Cells*, **18**, 270 (2018).
11. N. Nonoyama, S. Okazaki, A. Z. Weber, Y. Ikogi, and T. Yoshida, "Analysis of oxygen-transport diffusion resistance in proton-exchange-membrane fuel cells." *J. Electrochem. Soc.*, **158**, B416 (2011).
12. M. Eikerling and A. A. Kulikovsky, *Polymer Electrolyte Fuel Cells Physical Principles of Materials and Operation* (CRC Press, Boca Raton, FL) (2014).
13. M. Eikerling, A. A. Kornyshev, and A. R. Kucernak, "Water in polymer electrolyte fuel cells: Friend or foe? " *Phys. Today*, **59**, 38 (2006).
14. M. Tesfaye, A. N. MacDonald, P. J. Dudenas, A. Kusoglu, and A. Z. Weber, "Exploring substrate/ionomer interaction under oxidizing and reducing environments." *Electrochem. Commun.*, **87**, 86 (2018).
15. M. Eikerling, "Water management in cathode catalyst layers of PEM Fuel Cells." *J. Electrochem. Soc.*, **153**, E58 (2006).
16. H. Li et al., "A review of water flooding issues in the proton exchange membrane fuel cell." *J. Power Sources*, **178**, 103 (2008).
17. D. Harvey, J. G. Pharoah, and K. Karan, "A comparison of different approaches to modelling the PEMFC catalyst layer." *J. Power Sources*, **179**, 209 (2008).
18. L. You and H. Liu, "A two-phase flow and transport model for the cathode of PEM fuel cells." *Int. J. Heat Mass Transfer*, **45**, 2277 (2002).
19. L. You and H. Liu, "A parametric study of the cathode catalyst layer of PEM fuel cells using a pseudo-homogeneous model." *Int. J. Hydrogen Energy*, **26**, 991 (2001).
20. M. H. Eikerling, K. Malek, and Q. Wang, "Catalyst layer modeling: structure, properties and performance." *PEM Fuel Cell Electrocatalysts and Catalyst Layers: Fundamentals and Applications*, ed. J. Zhang (Springer, London) p. 381 (2008).
21. Z. W. Seh, J. Kibsgaard, C. F. Dickens, I. Chorkendorff, J. K. Nørskov, and T. F. Jaramillo, "Combining theory and experiment in electrocatalysis: insights into materials design." *Science*, **355**, eaad4998 (2017).
22. K. Malek, T. Mashio, and M. Eikerling, "Microstructure of catalyst layers in PEM fuel cells redefined: a computational approach." *Electrocatalysis*, **2**, 141 (2011).
23. T. Mashio, A. Ohma, and T. Tokumasu, "Molecular dynamics study of ionomer adsorption at a carbon surface in catalyst ink." *Electrochim. Acta*, **202**, 14 (2016).
24. R. Jinnouchi, K. Kudo, N. Kitano, and Y. Morimoto, "Molecular dynamics simulations on O2 permeation through nafion ionomer on platinum surface." *Electrochim. Acta*, **188**, 767 (2016).
25. Y. Kurihara, T. Mabuchi, and T. Tokumasu, "Molecular dynamics study of oxygen transport resistance through ionomer thin film on Pt surface." *J. Power Sources*, **414**, 263 (2019).
26. A. Lerf, H. He, M. Forster, and J. Klinowski, "Structure of graphite oxide revisited." *J. Phys. Chem. B*, **102**, 4477 (1998).
27. D. B. Asay and S. H. Kim, "Evolution of the adsorbed water layer structure on silicon oxide at room temperature." *J. Phys. Chem. B*, **109**, 16760 (2005).
28. J. Bong, J. H. Park, T. Lim, S. J. Kang, S. K. Kwak, and S. Ju, "Contact angle analysis for the prediction of defect states of graphene grafted with functional groups." *Adv. Mater. Interfaces*, **5**, 1800166 (2018).
29. A. Malek and M. H. Eikerling, "Chemisorbed Oxygen at Pt(111): a DFT study of structural and electronic surface properties." *Electrocatalysis*, **9**, 370 (2018).
30. Q. He, N. S. Suraweera, D. C. Joy, and D. J. Keffer, "Structure of the ionomer film in catalyst layers of proton exchange membrane fuel cells." *The Journal of Physical Chemistry C*, **117**, 25305 (2013).
31. R. Sundararaman, K. Letchworth-Weaver, K. A. Schwarz, D. Gunceler, Y. Ozhabes, and T. A. Arias, "JDFTx: Software for joint density-functional theory." *SoftwareX*, **6**, 278 (2017).
32. S. Nishihara and M. Otani, "Hybrid solvation models for bulk, interface, and membrane: Reference interaction site methods coupled with density functional theory." *Physical Review B*, **96**, 115429 (2017).
33. A. Nouri-Khorasani, K. Malek, A. Malek, T. Mashio, D. P. Wilkinson, and M. H. Eikerling, "Molecular modeling of the proton density distribution in a water-filled slab-like nanopore bounded by Pt oxide and ionomer." *Catal. Today*, **262**, 133 (2016).
34. J. A. Spooner, M. J. Eslamibidigoli, K. Malek, and M. Eikerling, "Molecular dynamics study of the nanoscale proton density distribution at the ionomer-catalyst interface." *Pacific RIM Meeting on Electrochemical and Solid State Science*, I01A (2020).
35. A. Kusoglu, T. J. Dursch, and A. Z. Weber, "Nanostructure/swelling relationships of bulk and thin-film PFSA Ionomers." *Adv. Funct. Mater.*, **26**, 4961 (2016).
36. G. Kresse and J. Furthmüller, "Efficient iterative schemes for ab initio total-energy calculations using a plane-wave basis set." *Physical Review B*, **54**, 11169 (1996).
37. J. P. Perdew, K. Burke, and M. Ernzerhof, "Generalized gradient approximation made simple." *Phys. Rev. Lett.*, **77**, 3865 (1996).
38. P. E. Blöchl, "Projector augmented-wave method." *Physical Review B*, **50**, 17953 (1994).
39. B. Avasarala, R. Moore, and P. Haldar, "Surface oxidation of carbon supports due to potential cycling under PEM fuel cell conditions." *Electrochim. Acta*, **55**, 4765 (2010).
40. J. Lee, S. Escribano, F. Micoud, G. Gebel, S. Lyonnard, L. Porcar, N. Martinez, and A. Morin, "*In Situ* measurement of ionomer water content and liquid water saturation in fuel cell catalyst layers by high-resolution small-angle neutron scattering." *ACS Appl. Energy Mater.*, **3**, 8393 (2020).
41. K. Ito, T. Yamada, A. Shinohara, S.-I. Takata, and Y. Kawakita, "Dynamics of water in a catalyst layer of a fuel cell by quasielastic neutron scattering." *The Journal of Physical Chemistry C*, **125**, 21645 (2021).
42. N. Michaud-Agrawal, E. J. Denning, T. B. Woolf, and O. Beckstein, "MD analysis: a toolkit for the analysis of molecular dynamics simulations." *J. Comput. Chem.*, **32**, 2319 (2011).
43. H. J. C. Berendsen, D. van der Spoel, and R. van Dru[illegible]CS: a message-passing parallel molecular dynamics implementati[illegible]*ys. Commun.*, **91**, 43 (1995).
44. S. Páll, M. J. Abraham, C. Kutzner, B. Hess, and E. Lindahl, *Tackling Exascale Software Challenges in Molecular Dynamics Simulations with GROMACS* Solving Software Challenges for Exascale, ed. S. Markidis and E. Laure (Springer, Cham) p. 3 (2015).
45. G. Bussi, D. Donadio, and M. Parrinello, "Canonical sampling through velocity rescaling." *J. Chem. Phys.*, **126**, 014101 (2007).
46. T. Darden, D. York, and L. Pedersen, "Particle mesh ewald: an N·log(N) method for ewald sums in large systems." *J. Chem. Phys.*, **98**, 10089 (1993).
47. I.-C. Yeh and M. L. Berkowitz, "Ewald summation for systems with slab geometry." *J. Chem. Phys.*, **111**, 3155 (1999).
48. H. J. C. Berendsen, J. R. Grigera, and T. P. Straatsma, "The missing term in effective pair potentials." *J. Phys. Chem.*, **91**, 6269 (1987).
49. K. Toukan and A. Rahman, "Molecular-dynamics study of atomic motions in water." *Physical Review B*, **31**, 2643 (1985).
50. N. Schmid, A. P. Eichenberger, A. Choutko, S. Riniker, M. Winger, A. E. Mark, and W. F. van Gunsteren, "Definition and testing of the GROMOS force-field versions 54A7 and 54B7." *Eur. Biophys. J.*, **40**, 843 (2011).
51. J. R. Grigera, S. G. Kalko, and J. Fischbarg, "Wall−water interface. a molecular dynamics study." *Langmuir*, **12**, 154 (1996).
52. C. R. Randall, S. C. DeCaluwe, J. A. Dura, and L. Zou, "Quantifying the impacts of nafion interfaces with PEMFC relevant substrates using neutron reflectometry and modeling." *ECS-PRIME 2020 Joint International Meeting* (2020).
53. J. H. Lee, G. Doo, S. H. Kwon, H. Kang, S. Choi, S.-D. Yim, H.-T. Kim, and S. G. Lee, "Controlling ionomer film morphology through altering Pt catalyst surface properties for polymer electrolyte membrane fuel cells." *ACS Applied Polymer Materials*, **2**, 1807 (2020).
54. D. L. Wood, J. Chlistunoff, J. Majewski, and R. L. Borup, "Nafion structural phenomena at platinum and carbon interfaces." *J. Am. Chem. Soc.*, **131**, 18096 (2009).
55. Y. Ono, A. Ohma, K. Shinohara, and K. Fushinobu, "Influence of equivalent weight of ionomer on local oxygen transport resistance in cathode catalyst layers." *J. Electrochem. Soc.*, **160**, F779 (2013).
56. W. Xiao, Z. Xia, H. Li, R. Sun, S. Wang, and G. Sun, "Electrochemical interface optimization toward low oxygen transport resistance in high-temperature polymer electrolyte fuel cells." *Energy Technology*, **8**, 2000085 (2020).